Heating rate dependence of coercivity and microstructure of Fe-B-P-Cu nanocrystalline soft magnetic materials

Yohei Nomura[a, *], Jun Uzuhashi[b], Tatsuya Tomita[a], Toru Takahashi[a], Hidenori Kuwata[a], Taichi Abe[b], Tadakatsu Ohkubo[b], Kazuhiro Hono[b]

[a] *Tohoku Magnet Institute Co., Ltd., 11 Kitaya, Masuda, Natori, 981-1224, Japan*
[b] *National Institute for Materials Science, 1-2-1 Sengen, Tsukuba, 305-0047, Japan*
* Corresponding author. Tel.: +81-22-796-9720
E-mail address: nomura.yohei@tohoku-magnet-inst.com (Y. Nomura).

Abstract

The nanocrystalline structure and soft magnetic properties of melt-spun Fe-B-P-Cu ribbons are largely influenced by heating rates for crystallization of amorphous precursors. In this study, we investigated the structure and soft magnetic properties of $Fe_{84.8}B_{4.9}P_{9.5}Cu_{0.8}$ (P-rich) and $Fe_{84.8}B_{10.9}P_{3.5}Cu_{0.8}$ (B-rich) melt-spun ribbons crystallized at two different heating rates, 0.67 K/s and 6.7 K/s, using transmission electron microscopy (TEM) and atom probe tomography (APT). The P-rich ribbon shows smaller coercivity regardless of the heating rates, while the B-rich ribbon shows large heating rate dependence of the coercivity. APT analyses have revealed that the size of Cu clusters in the P-rich nanocrystalline ribbon is larger than that in the B-rich nanocrystalline ribbon while their number densities are nearly the same. Also, the high heating rate led to a larger size and higher Cu concentration of the Cu clusters in both samples, indicating that the Cu clusters are effective as nuclei for α-Fe only when they are larger than a critical size. The solute partitioning behaviors between α-Fe and residual amorphous phase determined by APT analyses are consistent with the tie-lines between α-Fe and liquid phase in a calculated Fe-P-B ternary phase diagram. P was found to segregate at amorphous/α-Fe interface, suggesting the grain growth is controlled by the volume diffusion of P in the amorphous phase during their crystallization process.

Keywords:
Nanocrystalline soft magnet; Rapid-solidification, Crystallization; Microstructure; Coercivity; Transmission electron microscopy

1. Introduction

For improving the energy efficiency of electric motors at high frequency ranges for automotive applications, nanocrystalline soft magnetic material receives revived interest as a potential substitute for electrical steel sheets. In general, nanocrystalline soft magnets show substantially lower core loss compared to electrical steels, because of their superior soft magnetic properties such as permeability and low coercivity as well as the small thickness of melt spun ribbons. The first nanocrystalline soft magnetic material invented by Yoshizawa *et al.* is the Fe-Si-B-Nb-Cu alloy that is crystallized from amorphous ribbon precursor [1]. In the nanocrystalline state, it exhibits very high permeability and low core loss. However, the saturation magnetic flux density of the nanocrystalline Fe-Si-B-Nb-Cu alloy was limited to 1.55 T because of the high concentration of Si in $D0_3$-Fe_3Si primary crystals [2]. Thereafter, several nanocrystalline soft-magnetic materials have been explored to attain higher saturation magnetic flux density [3-10]. For example, nanocrystalline Fe-Zr-B alloys developed by Suzuki *et al*. show higher saturation magnetic flux density of 1.70 T [3, 4]. However, the Fe-Zr-B nanocrystalline alloy and its derivatives are not industrially viable because the melt-spinning process to manufacture ribbon must be carried out under an inert gas atmosphere. For mass production of large-width ribbon, melt-spinning processability in air is indispensable.

Recently Makino *et al*. developed a nanocrystalline Fe-Si-B-P-Cu alloy with saturation magnetic flux density of as high as 1.94 T, which can be produced in air [5]. The coercivity of the melt-spun ribbon sharply decreases when crystallized at a heating rate higher than 6.7 K/s as the result of the formation of nanocrystalline microstructure composed of α-Fe and P and B enriched residual amorphous phase. The low coercivity together with the small thickness of melt-spun ribbon leads to substantial decrease in hysteresis loss compared to electrical steels, so the Fe-Si-B-P-Cu nanocrystalline ribbon is considered to be promising as an ultra-low loss soft-magnetic material.

One of the most important applications of the ultra-low loss soft magnetic material is the cores of energy efficient motors. For the production of a motor core, blanks are cut out from melt-spun ribbon, and then they are stacked in multi-layers. However, since nanocrystalline ribbons are brittle, blanks must be handled delicately during blanking and stacking. Therefore, it is advantageous to manufacture a core using ductile amorphous ribbons and then crystallize the stacked ribbons by a heat-treatment. In this case, controlled heat treatment of the amorphous stack is difficult because of the large volume of the core and the exothermic reaction of the crystallization reaction. As a result, the grain size of α-Fe in annealed stacked core cannot be kept as small as in a

ribbon sample, so that the coercivity of the stacked core cannot be reduced to the value that can be achieved in a small piece of ribbon sample.

In order to overcome this engineering problem for manufacturing a motor core using nanocrystalline soft magnetic material, the melt-spun ribbon must show excellent soft magnetic properties evey by annealing at the low heating rates that can be achieved by heating stacked core, e.g. 0.67 K/s. Recently, Urata *et al.* systematically investigated the correlation between the nanocrystalline structure and the coercivity of Fe-B-P-Cu melt-spun ribbons with various compositions, and found that sufficiently low coercivity can be obtained even at a low heating rate of 0.67 K/s by increasing the amount of P in the Fe- B-P-Cu amorphous alloy precursor [7, 11]. However, it is not clear why the increase in the amount of P led to the suppression of the heating rate dependence of the grain size.

Hence the aim of this study was to understand the reason why the P-rich sample maintains the grain size to be a few tens nm even in the crystallization at a low heating rate of 0.67 K/s. Based on the work by Urata *et al.*, two alloy compositions, $Fe_{84.8}B_{4.9}P_{9.5}Cu_{0.8}$ (P-rich) and $Fe_{84.8}B_{10.9}P_{3.5}Cu_{0.8}$ (B-rich), were selected in this study. Melt-spun ribbons of these two alloys were annealed in a temperature range from 543 K to 743 K at two different heating rates of 0.67 K/s or 6.7 K/s. The microstructures of these samples were observed with transmission electron microscopy (TEM) and atom probe tomography (APT) and their results are correlated with coercivities to clarify the reason why the soft magnetic properties of the P-rich alloy becomes insensitive to the heating rates.

2. Experimental

Two mixtures of $Fe_{84.8}B_{4.9}P_{9.5}Cu_{0.8}$ (P-rich) and $Fe_{84.8}B_{10.9}P_{3.5}Cu_{0.8}$ (B-rich) as shown in Table 1 were prepared by mixing iron (< 0.01 wt.% impurities), boron (< 0.5 wt.% impurities), iron phosphide (< 1 wt.% impurities), and copper (< 0.01 wt.% impurities). Each of them was heated in an alumina crucible under an argon atmosphere using a high-frequency induction-heating furnace to form homogeneous molten metal, and then it was solidified in the copper mold to form a 200 g ingot. The ingot was crushed into small pieces, and 30 g of the pieces was charged in a quartz crucible with a nozzle having an opening of 10 mm × 0.3 mm. The alloy pieces were melted in the quartz crucible by induction heating under an argon atmosphere, and was cast from the nozzle on to a spinning Cu wheel at a wheel rotation speed of 20 m/s to form an amorphous ribbon with a width of 10 mm and a thickness of 20 μm.

The amorphous ribbons were heated to annealing temperatures (T_a) at heating

rates of 0.67 K/s or 6.7 K/s using an infrared gold image furnace under an argon flow of 1.67×10^{-5} m^3/s. For consistency, both samples were kept at T_a for 600 s, then the ribbon samples were cooled to room temperature at a cooling rate of 0.2 to 0.5 K/s. The annealing temperature was varied from 543 K to 743 K. A thermal analyzer DSC8500 was used to determine the primary crystallization temperature, T_{x1}, the peak temperature of the primary crystallization, T_p, the primary crystallization heat, ΔH_1, the secondary crystallization temperature, T_{x2}, and the secondary crystallization heat, ΔH_2, of the amorphous ribbons. In the thermal analysis, samples were heated to 923 K at a heating rate of 0.67 K/s and 6.7 K/s under an argon gas flow in a platinum pan. From the balance between a high exothermic peak and a low heat resistance, the weight of the samples was about 20 mg and 3 mg to a heating rate of 0.67 K/s and 6.7 K/s, respectively. The coercivity H_c and saturation mass magnetization M_s were determined from a B-H curve using a BH tracer Model BHS-40 and a vibrating sample magnetometer VSM-P7-15 in the amorphous and nano-crystalline ribbons, respectively. The saturation mass magnetization M_s was converted to the saturation magnetic flux density B_s using a volumetric mass density $\rho = 7.5 \times 10^3$ kg/m^3. The remanence-to-saturation ratio, B_r/B_s, of the nanocrystalline ribbons was calculated by dividing the remanent flux density, B_r, obtained from the B-H curve in the BH tracer by the saturation magnetic flux density, B_s.

TEM observations were performed using a FEI Titan G2 80-200 and APT analyses were performed using CAMECA LEAP5000 XS. Specimens for the TEM observations and the APT analyses were prepared by the lift-out technique from the center of ribbon, 3 μm in depth from the free surface, using a focused ion beam (FIB) system, FEI Helios G4UX. The melt-spun ribbons were annealed at two heating rates to the annealing temperature of T_a in Fig. 1. APT analyses were carried out in a laser mode at a specimen temperature of 30 K and the laser pulse energy and pulse rate were 5 pJ and 250 kHz, respectively. Acquired APT data were analyzed using the CAMECA Integrated Visualization and Analysis Software (IVAS®).

3. Results and discussion

3.1. Annealing temperature and heating rate dependencies of coercivity

Fig. 1 (a) and (b) show coercivity (H_c) as functions of the annealing temperature at two different heating rates, 0.67 K/s (blank circle) and 6.7 K/s (filled circle) for the P-rich and B-rich ribbons. The dashed line and solid line are T_{x1} and T_{x2} measured by the thermal analysis at 0.67 K/s. The coercivity of as melt-spun ribbon (As-Q) is shown on the left axis as a blank circle. The T-H_c curves have two local

minimums. In the local minimum below T_{x1}, both ribbons are mostly amorphous and the low coercivity is originated from the structural relaxation in the amorphous ribbons. In the high-temperature local minimum above T_{x1}, both ribbons have a nanocrystalline structure. Although there are a few exceptional points, the coercivities of P-rich samples are in general lower than those of B-rich samples for both heating rates. One distinctive feature of the P-rich sample is that the heating-rate dependence of the coercivity above 650 K is much smaller compared to the B-rich sample. This means that the P-rich sample gives rise to lower coercivity regardless of the heating rates, which is a definite merit in applying these ribbons to motor core application. In order to understand the reason for the better soft magnetic properties and their heating rate dependence in the crystallized P-rich ribbon, the structures of the four samples indicated by the arrows in Fig. 1 (a) and (b) were analyzed using TEM and APT.

3.2. Microstructure of amorphous ribbons

The coercivity of nanocrystalline soft magnetic material is known to decrease in proportion to d_{av}^6 when average grain size, d_{av}, becomes smaller than the exchange length defined as $L_{ex}^0=(A/K_1)^{1/2}$, where A is exchange stiffness and K_1 is the magnetocrystalline anisotropy constant [12]. Since crystalline size and its distribution in crystallized ribbon is governed by the nucleation and growth of α-Fe primary crystals in an amorphous precursor, the presence of preexisting nuclei largely influences the nanocrystalline structure [13]. Fig. 2 shows dark field TEM (DF-TEM) images and selected area electron diffraction (SAED) patterns obtained from the center of the ribbons. The DF-TEM images of both ribbons show uniform contrast, indicating the absence of pre-existing nuclei. The SAED patterns show halo, indicating the amorphous structure. Thus, both as melt-spun ribbons as a whole are fully amorphous in structure. To further confirm the chemical homogeneity, elemental distributions in the as melt-spun ribbons were investigated by APT. Fig. 3 shows APT atom maps of P, B and Cu taken from the interior region of as melt-spun ribbons and the corresponding frequency distributions of P, B, Cu and Fe. The frequency distribution of each element is consistent with a binomial distribution, suggesting that each element is randomly distributed in both ribbons within the detection limit.

3.3. Crystallization of amorphous ribbons

The coercivity of the P-rich ribbon is lower than that of the B-rich ribbon after crystallization at the heating rate of 6.7 K/s. For the lower heating rate of 0.67 K/s, the coercivity of the B-rich ribbon becomes substantially higher, while the heating rate

dependence of coercivity for the P-rich ribbon is not as much as that for the B-rich ribbon (Fig. 1). In order to understand the reason for the difference in the heating rate dependence of the coercivity in these two alloys, the grain size distributions were measured by BF-TEM images for the two alloys annealed at two different heating rates as shown in Fig. 4. The figure also includes the average grain size, d_{ave}, and the standard deviation, σ. The difference in the size distributions of the four samples can be summarized as follows:

1. for the same heating rate, the P-rich nanocrystalline ribbon has smaller d_{ave} and σ (20.9±3.9 nm at 0.67 K/s and 17.1±3.2 nm at 6.7 K/s) compared to the B-rich ribbon (28.8±9.7 nm at 0.67 K/s and 23.2±5.1 nm at 6.7 K/s); hence H_c of P-rich sample is lower;
2. for the same alloy composition, the high heating rate (6.7 K/s) leads to smaller d_{ave} and σ as compared with the low heating rate (0.67 K/s); hence the lower H_c can be obtained at higher heating rate;
3. for the low heating rate (0.67 K/s), the grain size and the distribution in the P-rich ribbon is smaller compared to that of the B-rich ribbon, hence the P-rich ribbon shows lower coercivity even at the low heating rate.

When the exponents, n, in d_{av}^n are determined from the slopes of line segments for $\ln H_c$ plotted against $\ln d_{av}$, the P-rich and B-rich ribbons have exponents of 3.0 and 6.7, respectively. The microstructure and the coercivity of the B-rich ribbons are well correlated with each other as predicted by the original local anisotropy theory by Herzer, *i.e.*, $H_c \propto d_{av}^6$ for $d_{av} < L_{ex}^0 = (A/K_1)^{1/2}$ [12]. On the other hand, the P-rich ribbons have the relationship between d_{av} and H_c as predicted by an extended theory by Suzuki *et al.*, *i.e.*, $H_c \propto d_{av}^3$ [14]. Suzuki *et al.* concluded from the difference in remanence-to-saturation ratio, B_r/B_s, of 0.95 and 0.45 between nanocrystalline $Fe_{77}Si_{12.5}B_8Nb_{1.5}Cu_1$ and $Fe_{91}Zr_7B_2$ ribbons having exponents, n, of 3 and 6 that induced uniaxial anisotropies produce the difference between the exponents, n. However, the B_r/B_s range in the P-rich and B-rich ribbons is 0.027 to 0.20 smaller than the remanence-to-saturation ratio, B_r/B_s, of 0.45 in the nanocrystalline $Fe_{91}Zr_7B_2$ ribbon regardless of the difference in the exponents, n. Therefore, it is anticipated that the exponents, n, vary according to not only the induced uniaxial anisotropy but also the other factors. As another factor, A. S. Bolyachkin *et al.* paid attention to the size distribution and evaluated the exponent, n, using σ/d_{ave} [15]. The P-rich ribbons have the same σ/d_{ave} regardless of d_{av}, and the σ/d_{ave} of 0.19 corresponds with the exponent n of 3.0 according to Fig. 4 which Bolyachkin *et al.* provided. On the other hand, the B-rich ribbons have different values of σ/d_{ave} of 0.34 for d_{av}=28.8 nm and 0.22 for d_{av}=23.2 nm, and the difference in σ/d_{ave}

may cause the large exponent n=6.7 as expected from Fig. 3 of Bolyachkin *et al*. Therefore, it is crucial to use the same σ/d_{ave} in order to duly appreciate the exponent n. Interestingly, $Fe_{78}P_{9\text{-}16}C_{2\text{-}9}Ge_3Si_{0.5}Cu_{0.5}$ nanocrystalline alloys have the same exponent n=3 as the P-rich ribbon, which may imply that a high P content leads the same σ/d_{ave} [16]. "Note that the coercivity of the B-rich alloy heated at 6.7 K/s is smaller than that for the P-rich alloy heated at 0.67 K/s regardless of its larger grain size of 23.2 nm compared to 20.9 nm for the P-rich alloy. This is because coercivity depends not only on the average grain size and grain size distribution but also on the intrinsic magnetic properties of the constituent phases."

In order to evaluate the difference in the size distribution from the viewpoint of kinetics, the crystallization process of each amorphous ribbon was thermally analyzed by differential scanning calorimetry (DSC) at each heating rate of 0.67 K/s and 6.7 K/s as shown in Fig. 5. The amorphous phase crystallizes to the BCC Fe (α-Fe) phase by the primary crystallization mechanism at T_{x1}, which releases heat of ΔH_1. During the primary crystallization process, P and B are considered to be rejected from α-Fe and enriched in the residual amorphous phase as reported in Fe-Si-B-P-Cu alloy [17]. At T_{x2}, the residual amorphous phase crystallizes into Fe_2B and $Fe_3(P, B)$. This reaction emits heat of ΔH_2 during the crystallization. Table 2 shows T_{x1}, T_{x2}, ΔH_1 and ΔH_2 of both alloys. As to the samples annealed at the high heating rate of 6.7 K/s, ΔH_1 and ΔH_2 cannot be determined because of the lack of background data in a high temperature range above the temperature limit of the thermal analyzer. In the DSC curves, the glass transition temperature T_g does not appear.

For the kinetics analysis of the crystallization reaction, the Kissinger method is used as a simple method [18]. Assuming that the primary crystallization process consists of single elementary step and the accommodation function of rate equation is constant in the step, the rate equation is as follows:

$$dq/dt = A\exp(-E_a/RT)f(q) \quad , \tag{1}$$

where q is the fraction reacted, *i.e.*, the heat generation, t the time, A the pre-exponential factor, E_a the activation energy, R the gas constant, T the absolute temperature, $f(q)$ a function of the fraction reacted [18, 19]. Taking the differentiation of the rate equation and simplifying using a heating rate $\Delta T/t$, yields:

$$d^2q/dt^2 = (dq/dt)[(df(q)/dq)A\exp(-E_a/RT) + (\Delta T/t)E_a/RT^2]. \tag{2}$$

When the fraction reacted q is q_p at a peak temperature T_p, d^2q_p/dt^2 is zero and the following equation is obtained.

$$\ln((\Delta T/t)/T_p^2) = \ln[-(df(q_p)/dq_p)(AR/E_a)] - E_a/RT_p \tag{3}$$

The activation energy E_a is obtained from the slope of the least-squares regression line of best fit for $\ln((\Delta T/t)/T_p^2)$ plotted against $(-1/RT_p)$ (abscissa). Table 3 shows the activation energy E_a evaluated from the data of Fig. 5 as well as the peak temperature T_p, H_c, B_s, B_r/B_s, d_{ave} and σ.

There is no difference between the activation energies in the primary crystallization process of the P-rich and B-rich alloys (~139 kJ/mol), regardless of the large difference in the heating rate dependence of H_c and d_{ave}. In literature, the activation energies for the diffusion of P in α-Fe and an amorphous phase were reported to be 178 kJ/mol and 169 kJ/mol [20, 21]; hence the activation energy for the crystallization of α-Fe estimated in this work is slightly lower than the activation energy for the diffusion of P. However, it is not easy to determine the rate-controlling steps only from the thermal analysis. As the first step for determining the rate-controlling steps, we investigated the elemental distribution in the samples after the primary crystallization process using APT.

3.4. Solute partitioning in α-Fe/amorphous phases

Fig. 6 shows 2nm sliced APT atom maps of P, B and Cu atoms taken from the four crystallized samples and line concentration profiles of Fe, P, B and Cu atoms taken along the arrows in the selected volumes in the sliced APT atom maps. P and B lean regions correspond to α-Fe nanocrystals. The tendency of the size distribution of α-Fe in the ATP maps of Fig. 6 is consistent with that observed in the TEM images in Fig. 4. Table 4 shows the average concentration of Fe, P, B and Cu in α-Fe and the residual amorphous phase calculated from the line concentration profiles. The APT results have shown that the volume fractions of α-Fe phase, V_f, in the P-rich and B-rich samples are 60% and 50%, respectively. The P concentrations in the α-Fe crystals in the P-rich and B-rich samples are ~2.5 at.% and ~0.5-1 at.%. According to literature, the saturation magnetostrictions value for α-Fe containing 2-3 at.% P and 0.5-1 at.% P are around -4 ppm and -8 ppm [22]. Table 4 also shows the chemical composition of the residual amorphous phase for P-rich and B-rich samples are $Fe_{74}P_{16}B_9$ and $Fe_{76}P_4B_{19}$, respectively. Although the actual measurement results of the magnetostriction values for these amorphous alloys are not available, they should not be that far from the saturation magnetostriction value, λ_s, for amorphous $Fe_{80}P_{14}B_6$, which is reported to be around 26 ppm [20]. Then, using $\lambda_s^{eff} = V_f\lambda_s^c + (1-V_f)\lambda_s^a$, the saturation magnetostriction for the P-rich and B-rich nanocrystalline ribbons are roughly estimated to be 8 and 9 ppm [21]. This may be another reason for the lower coercivity of the nanocrystalline P-rich sample. Table 3 also shows the saturation magnetic flux density B_s of the crystallized

samples. The saturation magnetic flux density B_s becomes higher as the volume fraction V_f in the same chemical composition increases because the flux density B_s of α-Fe is higher than that of the amorphous phase. Although the P-rich sample had a higher volume fraction V_f as compared with B-rich sample, the flux density B_s of the P-rich sample is smaller than that of the B-rich sample. In literature, the substitution of B for P decreases the saturation magnetic moment of amorphous Fe-P-B alloys [20]. This may lead a decrease in magnetic flux density of the P-rich sample. However, the higher volume fraction V_f of α-Fe phase in the P-rich sample may suggest that the decrease is not so large.

In order to explain the partitioning behaviors of P and B between α-Fe/amorphous observed by APT, we have calculated the phase equilibria in the B-rich and the P-rich alloys slightly above T_{x1} using a thermodynamic calculation software, Thermo-Calc [22], with a database of TCFE version 9 [23]. Fig. 7 shows the calculated isothermal section of the Fe-B-P ternary system. Based on the DSC curves in Fig. 5 the temperature was selected to be 673 K, which is slightly above T_{x1}. In this calculation, Cu was excluded because it partitions to neither α-Fe nor the amorphous phase. So only α-Fe and a liquid phase were considered in the calculations where the Gibbs energy of liquid was used for the amorphous phase. In the P-rich alloy, the concentration of P in α-Fe is slightly higher than that in the B-rich alloy. This result is in good agreement with the APT atom maps in Fig. 6 and the quantitative analysis result in Table 4, *i.e.*, the concentrations of P in the α-Fe crystals in the P-rich and B-rich alloys are 2.6 and 0.47 at.%, respectively, for the heating rate of 6.7 K/s. The chemical composition of the residual amorphous phase in the P-rich alloy is ~$Fe_{74}P_{16}B_9$, while that in the B-rich alloy is ~$Fe_{76}P_4B_{19}$. This difference can also be explained from the tie-lines between α-Fe/liquid for each alloy composition; *i.e.*, the equilibrium concentration of the amorphous phase in the P-rich and B-rich samples are $Fe_{70}P_{16}B_{14}$ and $Fe_{68}P_2B_{30}$, which are qualitatively in agreement with the experimental values in Table 4. The slight enrichment of P at the α-Fe/amorphous interfaces in the concentration profiles in Fig. 6 may indicate that the grain growth is controlled by the volume diffusion of P in the amorphous phase.

3.5 Cu clusters

In all nanocrystalline ribbons, a large number density of Cu clusters is observed even within α-Fe crystals as well as in the residual amorphous phase. Regarding the Cu clusters in nanocrystalline soft magnetic materials, Hono *et al*. reported that the fcc Cu precipitates that develop from Cu clusters serves as heterogeneous nucleation sites for

α-Fe with the Krujumov-Sacks orientation relationship [24, 25]. Table 5 summarizes the number densities of Cu clusters, n_{Cu}, and the average diameters of the Cu clusters, d_{Cu}, which was evaluated by counting the number of spaces enclosed by a 2.3 at.% Cu iso-concentration-surface in each APT atom map in Fig. 6. Table 5 also includes the standard deviations of the diameters, σ_{Cu}, and the standard errors of the diameters, *SE*, of the Cu clusters. For the same heating rate, the P-rich ribbon has a smaller n_{Cu} and a larger d_{Cu} than those in the B-rich ribbon. The number density of Cu clusters in these four samples are all in the same order of 10^{24} m^{-3}; however, the number density for the B-rich alloy is 1.5 times larger than those for the P-rich alloy. This indicates that the grain size has nothing to do with the number density of the Cu clusters; hence, only a part of Cu clusters appears to be effective as heterogeneous nucleation sites for α-Fe. Note that the average size of Cu clusters, d_{Cu}, is larger in the P-rich alloys for the same heating rate. In particular, the Cu clusters in the P-rich ribbon annealed at the heating rate of 6.7 K/s is the largest of all, in which the grain size of α-Fe and the coercivity is the smallest.

Fig. 8 (top) shows 2nm sliced APT atom maps of selected regions from Fig. 6, and (bottom) shows iso-concentration-surfaces drawn at 10at.%Cu. d_{Cu} in the P-rich samples appears to be larger than those in the B-rich sample. The 10at.%Cu iso-concentration-surface shows most of the Cu clusters in the P-rich sample contain Cu larger than 10 at.%, while only parts of those contain Cu larger than 10 at.% in the B-rich sample. Note that most of the Cu clusters containing Cu larger than 10 at.% are located at α-Fe/amorphous interfaces, suggesting that they are in direct contact with α-Fe, indicating that they have served as nuclei for the α-Fe crystals. In the B-rich sample, several Cu clusters are observed even within α-Fe; however, their Cu concertation is lower than 10 at.%. These clusters are considered to have formed after the primary crystallization of α-Fe by the precipitation of supersaturated Cu in the α-Fe precipitate as reported by Chen *et al.* [26]. Ohnuma *et al.* also reported that Cu clustering must occur prior to the onset of the primary crystallization [27]. In Fig. 8 (c) and (d), a number of Cu clusters are observed within α-Fe crystals, indicating that Cu clustering occurred after the onset of the crystallization. This means that the clustering rate was not fast enough in the B-rich amorphous alloy. By observing Cu clusters in the amorphous precursor and nanocrystalline Fe-Si-B-Nb-Cu alloy, Hono *et al.* reported that the Cu-clusters that form in the amorphous precursor eventually transform to fcc Cu when its size grows, and these fcc-Cu serves as the heterogeneous nucleation sites for α-Fe [28]. Although the crystal structures in the Cu clusters in Fig. 7 were not confirmed, the Cu clusters filtered with 10at.%Cu iso-concentration-surface are

believed to be fcc-Cu which acted as heterogeneous nucleation sites for α-Fe. In fact, Nishijima reported the presence of fcc-Cu in similar alloy, $Fe_{85.2}Si_1B_9P_4Cu_{0.8}$, using X-ray absorption fine structure (XAFS) [29]. Since the number density of these nuclei is large, the crystal grain size of the P-rich alloy is considered to be refined by an increase in the number of the crystal grains resultant from a large number of nucleation sites. On the other hand, in the B-rich sample, most of the Cu clusters are immature to act as nuclei because of its low Cu concentration and hence the crystal grain size is much larger compared to the P-rich sample.

4. Conclusion

In order to investigate the underlying mechanism of the small heating rate dependence and lower coercivity of $Fe_{84.8}B_{4.9}P_{9.5}Cu_{0.8}$ (P-rich) melt-spun ribbon with respect to $Fe_{84.8}B_{10.9}P_{3.5}Cu_{0.8}$ (B-rich) melt-spun ribbon, we investigated nanocrystalline structure and atomic scale solute distribution of the ribbons crystallized at two different heating rates, 6.7 and 0.67 K/s, using TEM and APT. The chemical compositions of α-Fe nanocrystals and residual amorphous phases in the P-rich and B-rich ribbons were quantitatively determined by APT, which are in fair agreement with the calculated equilibrium tie-lines between α-Fe/amorphous phases at the crystallization temperature. In both alloys crystallized at the two heating rates, the number densities of Cu clusters are almost the same; however, the number of Cu clusters that can serve as heterogeneous nucleation sites for α-Fe crystals is larger in the P-containing alloy. This explains the smaller grain size in the P-rich composition regardless of the heating rates. The concentration profiles through α-Fe/amorphous interface determined by APT show P enrichment at the interface, suggesting that the P diffusion in the amorphous phase control the growth of the α-Fe nanocrystals.

Acknowledgments

This research did not receive any specific grant from funding agencies in the public, commercial, or not-for-profit sectors. The authors wish to thank the Makino project, Tohoku University, for lending experimental equipment.

References

1. Y. Yoshizawa, S. Oguma, K. Yamauchi, New Fe-based soft magnetic alloys composed of ultrafine grain structure, J. Appl. Phys. 64 (1988) 6044-6046. https://doi.org/10.1063/1.342149.
2. Y. Yoshizawa, K. Yamauchi, Magnetic properties of ultrafine crystalline (Fe-Cu_1-Nb_3)-Si-B quasi-ternary alloys and improvement of their magnetic properties by magnetic field annealing, J. Magn. Soc. Jpn. 13 (1989) 231-236. https://doi.org/10.3379/jmsjmag.13.231.
3. K. Suzuki, A. Makino, A. Inoue, T. Masumoto, Soft magnetic properties of nanocrystalline bcc Fe-Zr−B and Fe−M−B−Cu (M=transition metal) alloys with high saturation magnetization (invited), J. Appl. Phys. 70 (1991) 6232-6237. https://doi.org/10.1063/1.350006.
4. A. Makino, A. Inoue, T. Masumoto, Nanocrystalline soft magnetic Fe-M-B (M = Zr, Hf, Nb) alloys produced by crystallization of amorphous phase (overview), Mater. Trans., JIM, 36 (1995) 924-938. https://doi.org/10.2320/matertrans1989.36.924.
5. A. Makino, H. Men, T. Kubota, K. Yubuta, A. Inoue, New excellent soft magnetic FeSiBPCu nanocrystallized alloys with high Bs of 1.9 T from nanohetero-amorphous phase, IEEE Trans. Magn., 45 (2009) 4302-4305. https://doi.org/10.1109/TMAG.2009.2023862.
6. M. Ohta, Y. Yoshizawa, Magnetic properties of nanocrystalline $Fe_{82.65}Cu_{1.35}Si_xB_{16-x}$ alloys (x=0-7), Appl. Phys. Lett. 91 (2007) 062517-1-062517-3. https://doi.org/10.1063/1.2769956.
7. A. Urata, H. Matsumoto, S. Yoshida, A. Makino, Fe–B–P–Cu nanocrystalline soft magnetic alloys with high Bs, J. Alloys Compd. 509 (2011) S431-S433. https://doi.org/10.1016/j.jallcom.2010.12.104.
8. Y. L. Jin, X. D. Fan, H. Men, X. C. Liu, B. L. Shen, FePCCu nanocrystalline alloys with excellent soft magnetic properties, Sci. China, Technol. Sci. 55 (2012) 3419-3424. https://doi.org/10.1007/s11431-012-4928-0.
9. F. G. Chen, Y. G. Wang, Investigation of glass forming ability, thermal stability and soft magnetic properties of melt-spun $Fe_{83}P_{16-x}Si_xCu_1$ (x = 0, 1, 2, 3, 4, 5) alloy ribbons, J. Alloys Compd. 584 (2014), 377-380. http://dx.doi.org/10.1016/j.jallcom.2013.09.089.
10. R. Xiang, S. X. Zhou, B. S. Dong, G. Q. Zhang, Z. Z. Li, Y. G. Wang, The excellent soft magnetic properties and corrosion behaviour of nanocrystalline FePCCu alloys, J. Mater. Sci.: Mater. Electron. 25 (2014) 2979-2984.

https://doi.org/10.1007/s10854-014-1970-7.
11. A. Urata, M. Yamaki, H. Matsumoto, S. Yoshida, A. Makino, inventors; NEC tokin corporation, Tohoku university, assignee; Alloy composition, Fe-based nanocrystalline alloy, manufacturing method thereof, and magnetic parts, JP patent 6046357, 2016 Dec 14.
12. G. Herzer, Grain size dependence of coercivity and permeability in nanocrystalline ferromagnets, IEEE Trans. Magn. 26 (1990) 1397-1402. https://doi.org/10.1109/20.104389.
13. P. Sharma, X. Zhang, Y. Zhang, A. Makino, Competition driven nanocrystallization in high Bs and low coreloss Fe–Si–B–P–Cu soft magnetic alloys, Scr. Mater. 95 (2015) 3-6. https://doi.org/10.1016/j.scriptamat.2014.08.023.
14. K. Suzuki, G. Herzer, J. M. Cadogan, The effect of coherent uniaxial anisotropies on the grain-size dependence of coercivity in nanocrystalline soft magnetic alloys, J. Magn. Magn. Mater. 177-181 (1998) 949-950. https://doi.org/10.1016/S0304-8853(97)00987-6.
15. A. S. Bolyachkin, S. V. Komogortsev, Power-law behavior of coercivity in nanocrystalline magnetic alloys with grain-size distribution, Scr. Mater. 152 (2018) 55-58. https://doi.org/10.1016/j.scriptamat.2018.04.008.
16. Y. Fujii, H. Fujita, A. Seki, T. Tomida, Magnetic properties of fine crystalline Fe-P-C-Cu-X alloys, J. Appl. Phys. 70 (1991) 6241-6243. https://doi.org/10.1063/1.350008.
17. S. Jafari, A. Beitollahi, B. E. Yekta, T. Ohkubo, V. Budinsky, M. Marsilius, G. Herzer, K. Hono, Atom probe analysis and magnetic properties of nanocrystalline $Fe_{84.3}Si_4B_8P_3Cu_{0.7}$, J. Alloys Compd. 674 (2016) 136-144. http://dx.doi.org/10.1016/j.jallcom.2016.03.005.
18. H. E. Kissinger, Reaction kinetics in differential thermal analysis, Anal. Chem. 29 (1957) 1702-1706. https://doi.org/10.1021/ac60131a045.
19. N. Koga, J. M. Criado, Application of the Kissinger method to solid-state reactions with a particle size distribution, J. Min. Metall. 35B (1999) 171-186.
20. G. Edelin, C. Tete, Diffusion of P in amorphous $Fe_{85}B_{15}$, Scripta Metall. 15 (1981) 739-742. https://doi.org/10.1016/0036-9748(81)90011-9.
21. D. R. Baer, L. R. Pederson, M. T. Thomas, Phosphorus diffusion in Fe-Ni-based amorphous alloys, Mater. Sci. Eng. 48 (1981) 283-290. https://doi.org/10.1016/0025-5416(81)90014-8.
22. R. M. Bozorth, Ferromagnetism, Van Nostrand Reinhold Inc., New York, 1951, p. 680.

23. F. E. Luborsky, Amorphous ferromagnets, in: E. P. Wohlfarth (Ed.), Ferromagnetic Materials, Vol. 1, North Holland Publishing Co., Amsterdam, 1980, p. 451-529.
24. K. Twarowski, M. Kuźmiński, A. Ślawska-Waniewska, H. K. Lachowicz, G. Herzer, Magnetostriction of $Fe_{73.5}Cu_1Nb_3Si_{15.5}B_7$ nanocrystalline alloy, J. Magn. Magn. Mater. 140-144 (1995) 449-450. https://doi.org/10.1016/0304-8853(94)00729-2.
25. J.O. Andersson, T. Helander, L. Höglund, P. F. Shi, B. Sundman, Thermo-Calc & DICTRA, computational tools for materials science, Calphad 26 (2002) 273-312. https://doi.org/10.1016/S0364-5916(02)00037-8.
26. Thermo-Calc Software TCFE Steels/Fe-alloys database version 9 (accessed 17 July 2020).
27. K. Hono, Nanoscale microstructural analysis of metallic materials by atom probe field ion microscopy, Prog. Mater. Sci. 47 (2002) 621-729. https://doi.org/10.1016/S0079-6425(01)00007-X.
28. T. Ohkubo, H. Kai, D. H. Ping, K. Hono, Y. Hirotsu, Mechanism of heterogeneous nucleation of α-Fe nanocrystals from $Fe_{89}Zr_7B_3Cu_1$ amorphous alloy, Scripta Mater. 44 (2001) 971. https://doi.org/10.1016/S1359-6462(00)00689-8.
29. Y. M. Chen, T. Ohkubo, M. Ohta, Y. Yoshizawa, K. Hono, Three-dimensional atom probe study of Fe-B-based nanocrystalline soft magnetic materials, Acta Mater. 57 (2009) 4463-4472. https://doi.org/10.1016/j.actamat.2009.06.008.
30. M. Ohnuma, D. H. Ping, T. Abe, H. Onodera, K. Hono, Optimization of the microstructure and properties of Co-substituted Fe-Si-B-Nb-Cu nanocrystalline soft magnetic alloys, J. Appl. Phys. 93 (2003) 9186-9194. https://doi.org/10.1063/1.1569396.
31. K. Hono, D. H. Ping, M. Ohnuma, H. Onodera, Cu clustering and Si partitioning in the early crystallization stage of an $Fe_{73.5}Si_{13.5}B_9Nb_3Cu_1$ amorphous alloy, Acta mater. 47 (1999) 997-1006. https://doi.org/10.1016/S1359-6454(98)00392-9.
32. M. Nishijima, M. Matsuura, K. Takenaka, A. Takeuchi, H. Ofuchi, A. Makino, Phase transition from fcc to bcc structure of the Cu-clusters during nanocrystallization of $Fe_{85.2}Si_1B_9P_4Cu_{0.8}$ soft magnetic alloy, AIP Adv. 4 (2014) 057129-1-057129-7. https://doi.org/10.1063/1.4880241.

Table 1. The chemical composition of P-rich and B-rich alloys.

No.	Fe	B	P	Cu
	at.%			
P-rich	84.8	4.9	9.5	0.8
B-rich	84.8	10.9	3.5	0.8

Table 2. T_{x1}, T_{x2}, ΔH_1 and ΔH_2 obtained from the DSC curves of Fig. 5.

No.	$\Delta T/t$	T_{x1}	T_{x2}	ΔH_1	ΔH_2
	K/s	K	K	J/g	J/g
P-rich	0.67	657	664	111	50
	6.7	707	730	N.A.	N.A.
B-rich	0.67	680	689	132	55
	6.7	734	759	N.A.	N.A.

Table 3. T_p and E_a obtained from the DSC curves in Fig. 5 and the relationship between $(-1/RT_p)$ and $\ln((\Delta T/t)/T_p^2)$, respectively.

No.	$\Delta T/t$	T_a	H_c	B_s	B_r/B_s	d_{ave}	σ	T_p	E_a
	K/s	K	A/m	T	-	nm	nm	K	kJ/mol
P-rich	0.67	663	9.0	1.70	0.047	20.9	3.9	664	129
	6.7	683	4.9	1.71	0.20	17.1	3.2	730	
B-rich	0.67	683	35.5	1.76	0.027	28.8	9.7	689	131
	6.7	703	8.4	1.77	0.047	23.2	5.1	759	

Table 4. The average concentration of Fe, P, B and Cu in α-Fe and the retained amorphous phase and the volume fraction V_f of both phases.

No.	$\Delta T/t$	Phase	Fe	P	B	Cu	V_f	ΔH_1
	K/s		at.%	at.%	at.%	at.%	%	J/g
P-rich	0.67	α-Fe	96.6	2.5	0.44	Bal.	59.6	111
		Amorphous	73.7	16.0	9.2	Bal.	40.4	
P-rich	6.7	α-Fe	96.2	2.6	0.56	Bal.	60.8	N.A.
		Amorphous	74.5	17.0	8.2	Bal.	39.2	
B-rich	0.67	α-Fe	97.7	0.97	0.85	Bal.	49.1	132
		Amorphous	75.9	4.2	19.1	Bal.	50.9	
B-rich	6.7	α-Fe	98.5	0.47	0.89	Bal.	52.6	N.A.
		Amorphous	71.1	6.9	21.7	Bal.	47.4	

Table 5. The number densities n_{Cu} and average diameter d_{Cu} of Cu clusters.

	$\Delta T/t$	T_a	H_c	d_{ave}	n_{Cu}	d_{Cu}	σ_{Cu}	*SE*
	K/s	K	A/m	nm	x10^{24} /m^3	nm	nm	nm
P-rich	0.67	663	9.0	20.9	2.2	3.24	1.02	0.06
	6.7	683	4.9	17.1	2.0	3.80	1.21	0.08
B-rich	0.67	683	35.5	28.8	3.0	2.94	0.88	0.04
	6.7	703	8.4	23.2	2.9	3.20	0.99	0.07

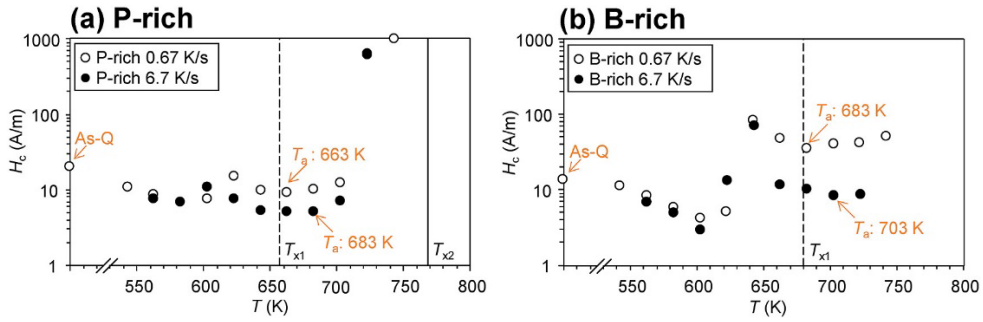

Fig. 1. The relationships between the maximum temperature and the coercivity after annealing the P-rich (a) and B-rich (b) amorphous ribbons.

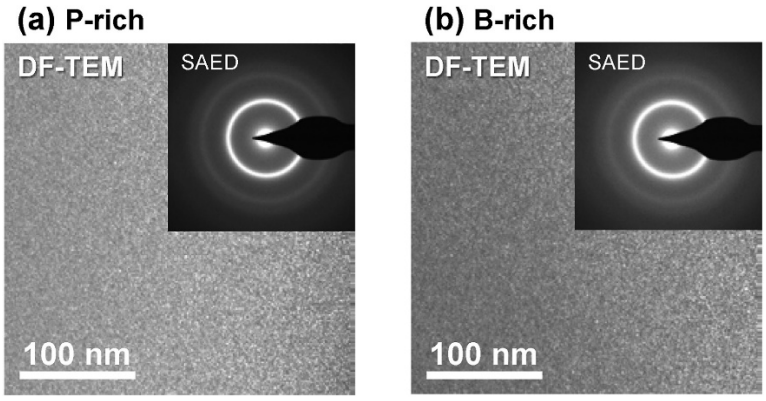

Fig. 2. Typical DF-TEM images and SAED patterns obtained from the P-rich amorphous ribbon (a) and from the B-rich amorphous ribbon (b).

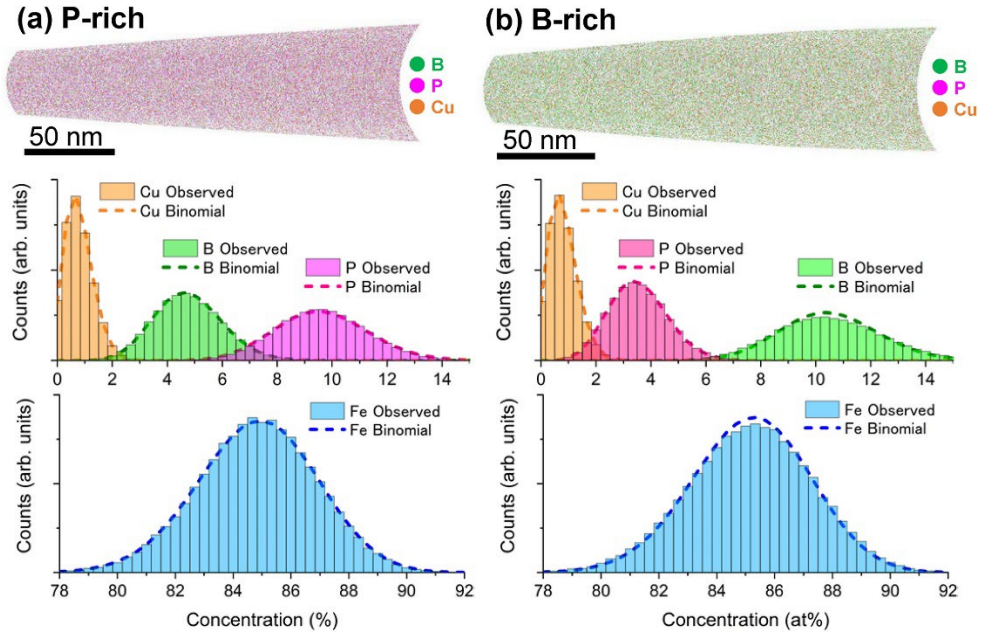

Fig. 3. 2 nm sliced APT atom maps of B, P, and Cu and frequency distributions of B, P, Cu and Fe obtained from the (a) P-rich and (b) B-rich amorphous ribbons.

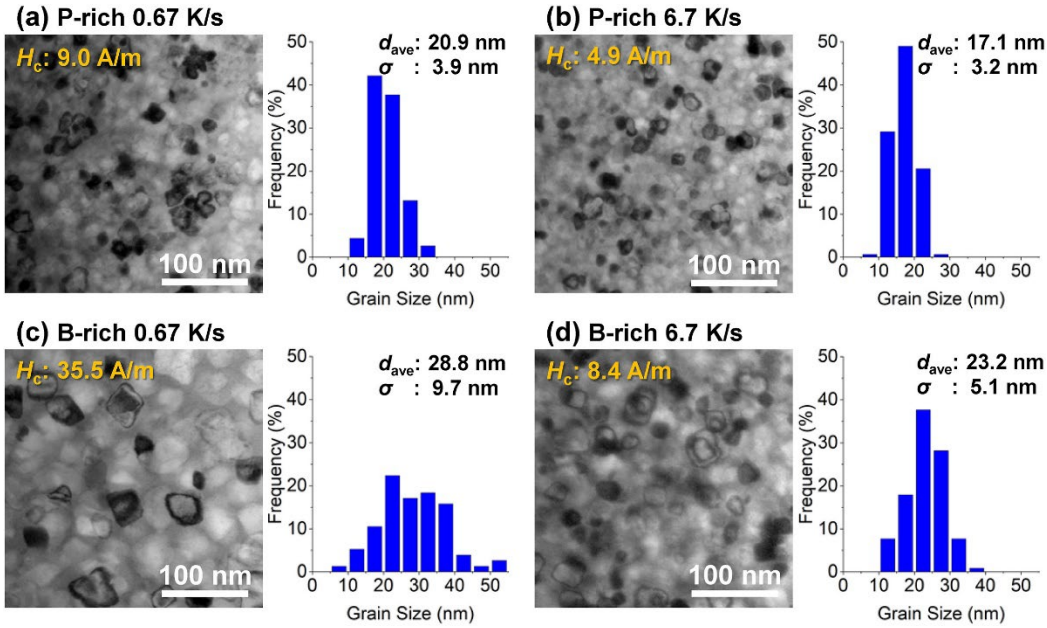

Fig. 4. BF-TEM images and size distributions of α-Fe grains of the P-rich nanocrystalline ribbon annealed at a low heating rate (0.67 K/s) (a) and a high heating rate (6.7 K/s) (b), and also the B-rich nanocrystalline ribbon annealed at a low heating rate (0.67 K/s) (c) and a high heating rate (6.7 K/s) (d).

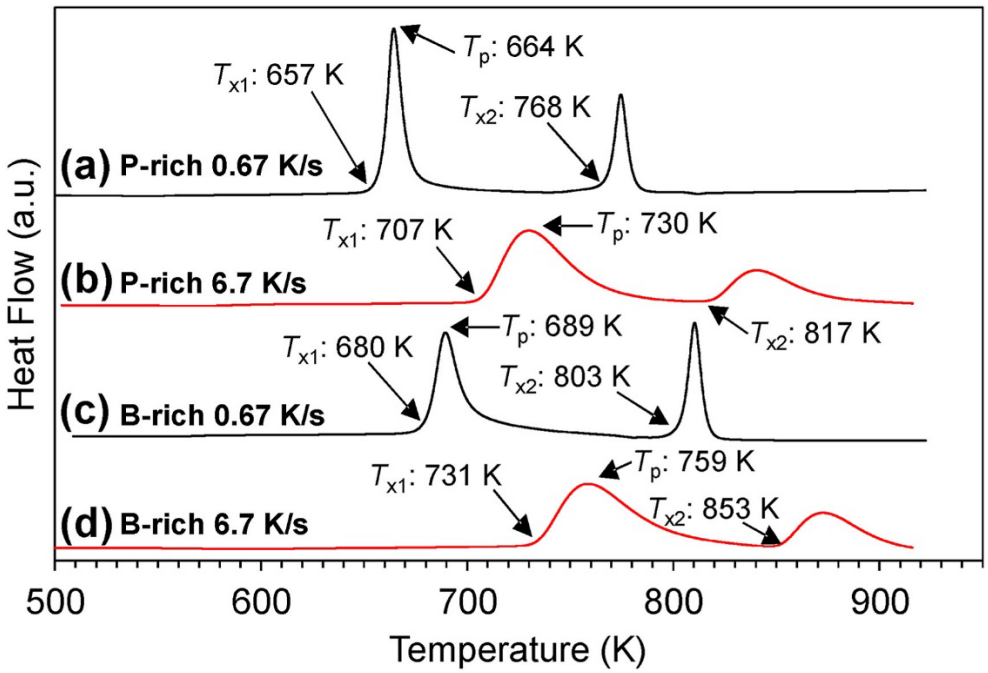

Fig. 5. DSC curves of the P-rich and B-rich amorphous ribbons. The P-rich alloy annealed at a low heating rate (0.67 K/s) (a) and a high heating rate (6.7 K/s) (b), and the B-rich alloy annealed at a low heating rate (0.67 K/s) (c) and a high heating rate (6.7 K/s) (d).

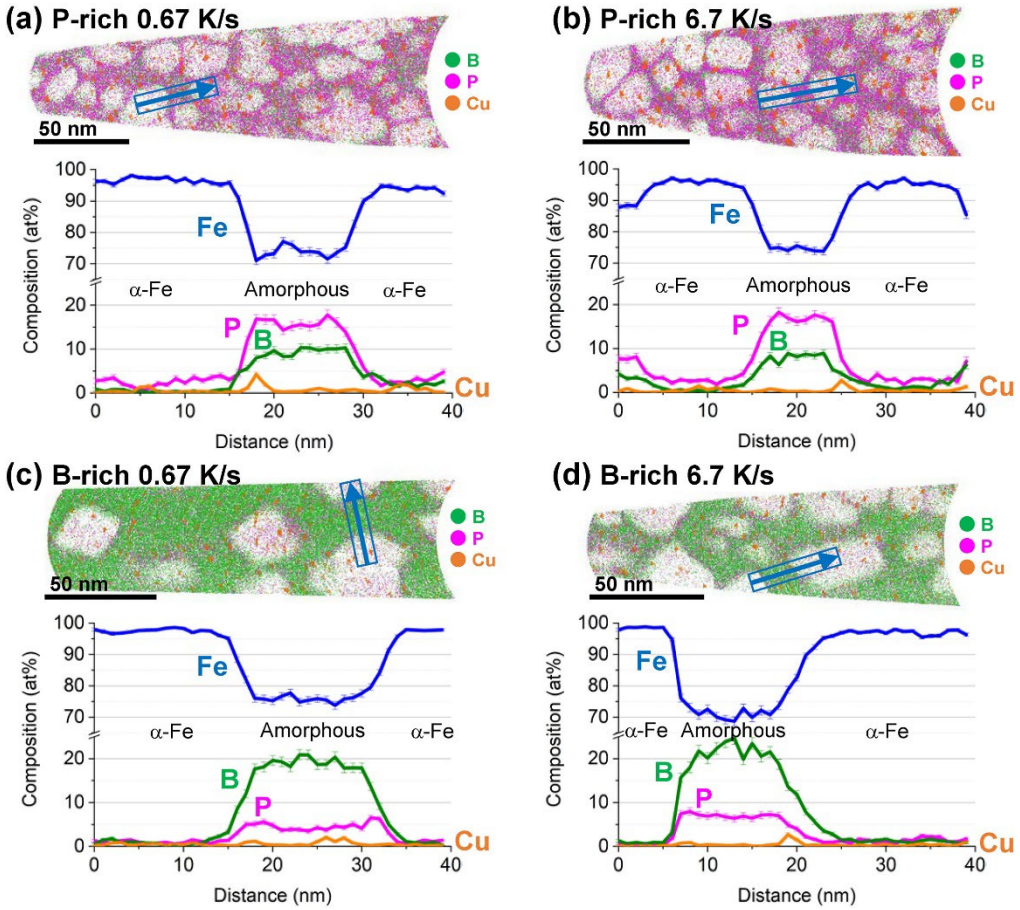

Fig. 6. 2nm sliced APT atom maps of P, B and Cu atoms and line concentration profiles of Fe, P, B and Cu atoms along an arrow.

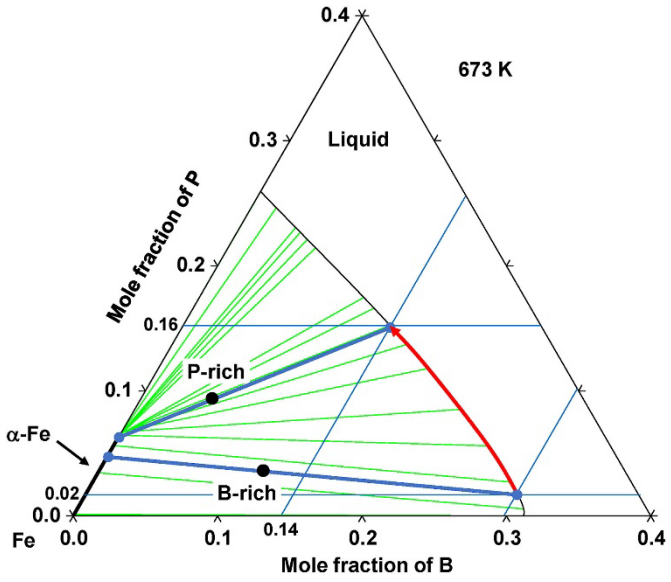

Fig. 7. Isothermal section of the Fe-B-P ternary system at 673 K calculated on Thermo-Calc with TCFE9 database, where the only liquid and α-Fe phases are considered.

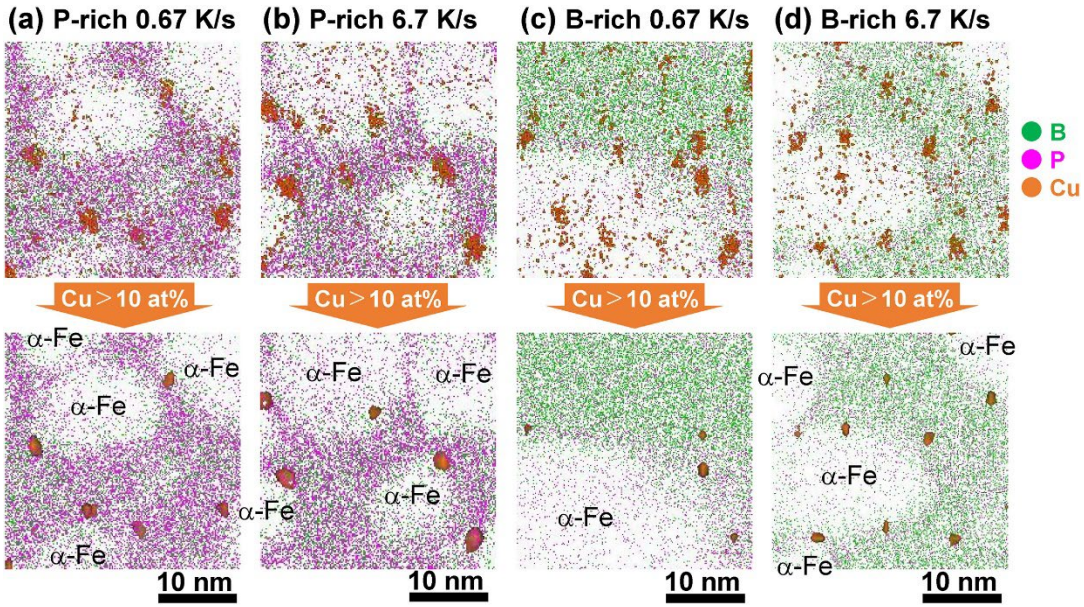

Fig. 8. Top images show 2nm sliced APT atom maps of B, P, and Cu. Only the Cu clusters containing >10 at.% Cu are shown in bottom images using iso-concentration-surfaces of Cu (threshold: 10 at.%).